World Journal of Mechanics, 2026, 16(9), 101-118
https://www.scirp.org/journal/wjm
ISSN Online: 2160-0503
ISSN Print: 2160-049X

Static Response and Load Transfer of a UH121 Upright-Piano Soundboard under Full-String Downbearing: A Finite Element Study

Wei Xiao[1], Wei Su[2]*, Chengzhong Gong[1]

[1]Guangzhou Pearl River Kayserburg Piano Co., Ltd., Guangzhou, China
[2]School of Aeronautics and Astronautics, Sun Yat-sen University, Shenzhen, China
Email: *suwei@mail.sysu.edu.cn

How to cite this paper: Xiao, W., Su, W. and Gong, C.Z. (2026) Static Response and Load Transfer of a UH121 Upright-Piano Soundboard under Full-String Downbearing: A Finite Element Study. *World Journal of Mechanics*, **16**, 101-118.
https://doi.org/10.4236/wjm.2026.169006

Received: August 14, 2026
Accepted: September 13, 2026
Published: September 16, 2026

Abstract

Static downbearing reaches the piano soundboard through the bridges; the resulting structural state reflects both broad panel bending and local redistribution around ribs and other stiffness transitions. To examine these two response scales, a three-dimensional linear-static finite-element model of the soundboard-rib-bridge assembly of a UH121 upright piano was built in ANSYS Workbench. The global Z component of the full-string downbearing was mapped onto the bridge regions. Every one of the 438 source load points was transferred, and the source and target Z-resultants were both −6413.5 N. Maximum total deformation was 1.4251, 1.5045, and 1.4551 mm for the coarse, baseline, and fine meshes, respectively; none differed from the fine-mesh value by more than 3.40%. In the baseline model, Z displacement extended from −1.5045 to 0.01265 mm. The maximum and minimum principal stresses reached 17.894 and −22.151 MPa, and the corresponding principal elastic-strain extrema were 1264.4 and −1420.2 με. The strongest local responses occurred near the bridges, ribs, bridge-rib neighborhoods, and constrained perimeter, rather than at the point of maximum displacement. Electrical strain measurements located a high-response region in a bridge-rib neighborhood, providing qualitative experimental support for the spatial pattern predicted by the model. The soundboard response was consequently characterized by global Z-direction bending superimposed on local load redistribution: the bridges introduced the load, whereas the panel and ribs carried it toward the surrounding structure. This static description can support subsequent assessment of upright-piano soundboards and rib configurations.

Keywords

Piano Soundboard, Static Downbearing, Finite-Element Analysis, Ribs, Load Transfer

1. Introduction

Viewed structurally, the piano soundboard is the load-bearing link between string excitation and radiation by the instrument body. The bridges introduce the string forces, but their eventual distribution depends on the combined stiffness of the orthotropic panel, ribs, bridge stiffening, and irregular perimeter. Rib spacing and arrangement have been associated with changes in local stiffness and vibration localization, while the bridges add a spatial filtering effect. A homogeneous-plate representation consequently misses important features of load transfer in an actual soundboard [1]-[4]. Parametric and physically based investigations also indicate that interpretable numerical predictions require explicit descriptions of the panel, ribs, bridges, geometry, and material properties [5]. Most of that work addresses dynamics or acoustics; in playing condition, however, the structure must first sustain the static downbearing produced by string tension. The accompanying pre-deformation, response gradients, and redistribution of load define the structural state on which later vibration develops.

Because a soundboard combines several interacting load-bearing components, both finite-element and analytical approaches have been used to describe its behavior. Berthaut *et al.* coupled a soundboard-rib-bridge model with experimental modal analysis to examine orthotropy, stiffening, and boundary representation [6]. Work on upright-piano soundboards has likewise paired finite-element analysis with computer-aided design when considering material properties, geometry, and rib layout [7] [8]. For non-rectangular orthotropic ribbed panels, the analytical and finite-element formulations developed by Trévisan *et al.* clarified how ribs and bridges partition the structural response [9] [10]. A more recent comparison of soundboard representations in string-soundboard coupling models reached a related conclusion: choices made when simplifying geometry, material behavior, or structural detail affect not only the predicted response but also the range over which the model remains applicable [11].

Manufacturing state and static downbearing form a second, closely related modeling problem. In the finite-element model of Mamou-Mani *et al.*, initial crown, ribs, bridges, and downbearing were represented together; the analysis showed that geometric stiffness and large-displacement treatment influence the prestressed state and the dynamic predictions derived from it [12]. Tests on a simplified string-instrument soundboard also found that prestress associated with crown and downbearing can alter modal properties [13]. Corradi *et al.* followed bonding, crown, and residual stress through successive manufacturing stages and compared the resulting model with experimental modal data [14]. Parametric finite-element studies have meanwhile considered crown, downbearing, geometric nonlinearity, and structural sensitivity [15]. These contributions make the importance of geometry, downbearing, and construction detail clear, yet their endpoints remain predominantly dynamic. Deformation, stress/strain, and load transfer in a complete upright piano carrying the static load of all strings have received much less direct attention.

Experimental checks of piano-soundboard models have usually relied on natural frequencies, mode shapes, mobility, or string response [2] [3] [6] [9] [11] [14] [16]. Those measurements are well-suited to dynamic model assessment, but they say less about deformation, local stress/strain, and the route followed by full-string static downbearing through a complete upright-piano soundboard. Direct access to an assembled instrument is also restricted, so a static experiment inevitably samples only selected locations. Used together, finite-element analysis and electrical strain measurement can bridge these scales: the calculation resolves the global bending field, while the gauges indicate where strong local responses actually occur.

Against this background, a three-dimensional static finite-element model was developed for the soundboard-rib-bridge assembly of a UH121 upright piano, with the vertical downbearing from all strings applied to the bridges. The analysis addressed four questions: how the assembly bends globally in the Z direction; where principal stress and principal strain become concentrated around bridges, ribs, and neighboring regions; how load passes from the bridges through the soundboard and ribs toward the perimeter; and whether the regional finite-element pattern is consistent with electrical strain measurements. Only static structural behavior is considered here; tone, sound radiation, and dynamic performance fall outside the stated scope.

2. Materials and Methods

2.1. Study Object and Numerical Environment

The object of analysis was the UH121 upright-piano soundboard-rib-bridge assembly subjected to the static downbearing generated by all strings. Calculations were performed in the Static Structural system of ANSYS Workbench, with ANSYS Mechanical/MAPDL used for the solution.

2.2. Geometry, Assembly, and Simplifications

The three-dimensional geometry included the macroscopic forms of the soundboard, ribs, and treble and bass bridges, and no symmetry reduction was introduced. The components were modeled as a continuously bonded assembly, with adhesive interfaces represented by perfectly bonded connections. Wood microstructure, explicit adhesive layers, and small geometric details were omitted so that the model retained the principal load-bearing parts and transfer paths without unnecessary geometric complexity.

The model geometry was reconstructed from the UH121 production CAD drawings. The soundboard measured-data drawing gives an overall reference envelope of 1429 mm ± 0.5 mm by 955 mm ± 0.5 mm and specifies a nominal finished thickness of 8 mm, with a local 7 mm middle-register area noted on the drawing. Eleven ribs were represented. Their nominal width × height dimensions from ribs 1 to 11 were 20 × 19, 20 × 20, 22 × 20, 22 × 20, 24 × 23, 25 × 27, 25 × 25, 24 × 22, 22 × 20, 20 × 19, and 20 × 19 mm; the corresponding nominal lengths were 348, 506, 665, 823, 989, 1110, 996, 891, 786, 682, and 577 mm. The production-drawing nominal dimensions were retained in the final simplified FE geometry for the represented load-bearing components; no dimensional substitutions or offsets were introduced. Differences were limited to the explicitly stated omission of small manufacturing details and the flat initial-soundboard assumption.

The bridge part drawings show layered and locally varying sections rather than uniform rectangular members. In drawing UH121, representative paired widths of 35/22 mm and 32/20 mm are marked for the middle-register and treble component profiles, respectively; local section labels are 4.5 mm in the middle register and 4.25 mm in the treble region. A representative bass-bridge section in drawing UH121 is 30 mm wide and 25 mm high, with a 16 mm central member and two 7 mm shoulders. The CAD profiles, not a single equivalent rectangle, were the geometric basis; drilling, fasteners, and other small manufacturing details were omitted from the FE model.

Manufacturing prestress, the sequence in which string tension was introduced, and self-weight were not represented. Moisture evolution, damage to the material, adhesive debonding, and failure were also beyond the intended analysis. Accordingly, the calculated fields describe the prescribed geometry under linear-elastic behavior, idealized connections, a peripheral constraint, and a vertical static load.

2.3. Governing Equations and Constitutive Law

A three-dimensional small-deformation, linear-elastic static formulation was adopted for the baseline calculation, following the standard equations of linear elasticity [17] [18]. After neglecting body force, the equilibrium over the domain Ω took the form

$$\nabla \cdot \sigma = 0 \tag{1}$$

with

$$u = \bar{u} \quad \text{on } \Gamma_u \tag{2a}$$

$$\sigma n = \bar{t} \quad \text{on } \Gamma_t \tag{2b}$$

The infinitesimal strain tensor was

$$\varepsilon = \frac{1}{2}\left(\nabla u + \nabla u^{\mathrm{T}}\right) \tag{3}$$

and the current solver used an isotropic linear-elastic law,

$$\sigma = \lambda \operatorname{tr}(\varepsilon) I + 2G\varepsilon \tag{4}$$

where $G = \frac{E}{2(1+\nu)}$ and $\lambda = \frac{E\nu}{(1+\nu)(1-2\nu)}$. With $E = 14150$ MPa and $\nu = 0.328$, $G \approx 5327.56$ MPa and $\lambda \approx 10159.53$ MPa. The discretized equilibrium equation was $Ku = F$. A small-deformation linear-static formulation was used; geometric nonlinearity and manufacturing-prestress effects were outside the scope of this study [17] [18].

The maximum predicted deformation of 1.5045 mm is 0.105% of the drawing-based 1429 mm reference width and 0.158% of the 955 mm reference height. Relative to the nominal 8 mm finished thickness, the deformation-to-thickness ratio is 0.188; the drawing also notes a local 7 mm middle-register area, for which the corresponding ratio would be 0.215. The initial soundboard geometry was assumed flat; the initial crown was not represented. These ratios support the use of a first-order small-deformation baseline for the prescribed geometry, while not demonstrating that crown and manufacturing prestress are negligible. Their omission can alter the initial geometry, tangent stiffness, and local load redistribution; the reported solution should therefore be interpreted as a linear static baseline rather than a complete prestressed-state prediction.

2.4. Material Model and Properties

The soundboard, ribs, and bridges were represented by a homogeneous isotropic linear-elastic material with Young's modulus $E = 14150$ MPa and Poisson's ratio $\nu = 0.328$. The same elastic constants were used for nominal-stress conversion of the electrical measurements, ensuring a consistent elastic-parameter basis for the numerical and experimental descriptions.

The effective constants were obtained from material-mechanical-property testing performed by the manufacturer on wood specimens associated with the UH121 project. The final FE material parameters and the nominal-stress conversion of the strain-gauge measurements used the same effective elastic constants. They were applied as a common effective basis for the homogeneous isotropic baseline. This uniform assignment is a modeling simplification rather than an assertion that the soundboard, ribs, and bridges have identical orthotropic properties; component-specific material sets would be required for quantitative prediction of local stress.

Using one effective modulus provides a common static baseline for the existing assembly, but it cannot reproduce the different longitudinal, transverse, and through-thickness stiffnesses of wood. Interpretation was therefore centered on global deformation, the spatial extent of response regions, and the paths along which load was transferred. Local stress maxima were retained as indicators of response localization, not treated as material-strength limits.

2.5. Constraints and String-Downbearing Load

All translational degrees of freedom were constrained in the peripheral support region ($U_X = U_Y = U_Z = 0$). This boundary condition idealized the attachment of the soundboard to the piano structure as a fixed support.

The fully fixed perimeter was selected as an upper-restraint idealization of the glued attachment to the surrounding piano structure. It establishes a stable baseline but does not represent the finite translational and rotational compliance of the real support. No alternative-boundary sensitivity calculation was performed; consequently, global compliance and especially response features close to the constrained perimeter are boundary-condition dependent.

Imported Load was used to place the string load on the loaded surfaces of the treble and bass bridges, with only the global F_Z component retained. The mapping transferred all 438 source load points to 1,882 target nodes, giving a 100% mapping rate. Both the source and target Z-resultants were −6413.5 N, and the scale factor remained 1.0. When the 1,882 F_Z commands were summed directly, the result was −6413.464969 N; its 0.000546% difference from the displayed resultant shows that the mapping preserved the applied force.

The 438 source loads comprised 344 points along the treble bridge and 94 along the bass bridge, with downward Z-resultant magnitudes of 5004.811107 and 1408.653862 N, respectively. The instrument has 219 physical strings. Each string passes over two bridge pins inserted into the bridge, so the two pin contacts define two downward load locations and give 2 × 219 = 438 source points. For string i, the tension was obtained from the ideal-string relation $T = 4\mu L^2 f^2$, where f is the tuned fundamental frequency, L is the tabulated left-side string length, and μ is the linear mass density. With d_1 denoting the steel-core diameter, d_2 and d_3 the inner- and outer-winding diameters, and steel and copper densities of 7850 and 8820 kg/m^3, respectively, the archived calculation used the corresponding core-plus-helical-winding mass per unit length. The right-side string lengths and the in-plane string trajectories were read directly from the UH121 CAD drawing. The vertical components at the two pins were resolved from the adjacent string-segment tensions and inclinations determined from the bridge-to-reference height differences H and h, with downward force taken as negative global Z. Only F_Z was retained because the present analysis isolates static downbearing normal to the modeled soundboard; in-plane components and their potential bridge axial/shear effects were outside the model scope. The original per-string file containing the CAD-read right-side lengths and the intermediate pointwise angle calculations is no longer available. Although the cast-iron frame carries the dominant axial string tension, the horizontal deflection introduced by the bridge pins can transmit in-plane side-bearing forces and local force couples to the bridge. The present model retains only the global Z component to isolate normal static downbearing; these in-plane effects are therefore outside the current model scope.

2.6. Mesh and Numerical Solution

Three SOLID187 higher-order tetrahedral meshes were prepared. The coarse, baseline, and fine discretizations contained 82963 nodes/44371 elements, 161111 nodes/86598 elements, and 657691 nodes/378261 elements, respectively; nominal element sizes were 15 mm for the coarse mesh and 5 mm for the fine mesh. Mesh independence was judged mainly from the maximum total deformation, together with the spatial form of the displacement field. The three maximum values were 1.4251, 1.5045, and 1.4551 mm. Measured against the fine mesh, the coarse and baseline results differed by 2.06% and 3.40%, while the location of the high-deformation region and the overall bending pattern changed little. On that basis, the baseline mesh was used for the principal analyses, offering a practical balance between response stability and computational demand. The mesh data and deformation differences are summarized in Table 1.

Table 1. Three-level mesh comparison based on maximum total deformation.

Mesh	Nominal Size (mm)	Nodes	Elements	Maximum Total Deformation (mm)	Difference from Fine Mesh (%)
Coarse	15	82963	44371	1.4251	2.06
Baseline	Baseline Setting	161111	86598	1.5045	3.40
Fine	5	657691	378261	1.4551	—

Continuous displacement contours, spatial principal-stress and principal-strain fields, and conservation of the mapped load formed the main basis for interpretation. Isolated nodal maxima were retained only to locate high-response regions and were not read as evidence of material failure.

One static load step and one substep were used, ending at a load factor of 1.0. The symmetric PCG iterative solver handled the linear equations with a convergence tolerance of 10^{-8} and reached convergence after 209 iterations. The principal settings of the baseline model are summarized in Table 2.

Table 2. Principal settings of the baseline finite-element model.

Item	Model Setting	Description
Software	ANSYS Workbench/Mechanical/MAPDL	Static structural
Analysis	Three-dimensional linear statics; small deformation	Full-string static downbearing
Element and Mesh	SOLID187; 161111 nodes; 86598 elements	Higher-order tetrahedral discretization
Elastic Properties	$E = 14150$ MPa; $\nu = 0.328$	Homogeneous isotropic linear elasticity
Body Forces	Not applied	Self-weight and inertia excluded
Boundary	$U_X = U_Y = U_Z = 0$ at the perimeter	Idealized fixed support
Imported Load	Global F_Z only; −6413.5 N; 438/438 mapped	100% source-to-target mapping
Solver	Symmetric PCG; tolerance 10^{-8}; 209 iterations	Converged linear solution
Experimental Comparison	DH3818Y system; 77 measurement channels	76 valid channels; regional comparison

2.7. Post-Processing and Response Quantities

Post-processing covered total deformation, global Z displacement, maximum and minimum principal stress, von Mises equivalent stress, and maximum and minimum principal elastic strain. Global bending was described from total deformation and Z displacement; principal stress and strain were examined to locate responses near the bridges, ribs, stiffness transitions, and constrained perimeter. Reading these fields alongside the mapped load made it possible to trace load passage from the bridges into the soundboard, nearby ribs, and peripheral region. The equivalent stress field was kept as a secondary marker of multiaxial response rather than used as a wood-failure criterion.

2.8. Electrical Strain Measurement

Local response of the UH121 soundboard under full-string static loading was examined by electrical strain measurement. Four computer-based DH3818Y strain-acquisition units, each with 24 channels, communicated with a computer through an Ethernet switch. The 120 Ω resistance gauges were connected in quarter-bridge circuits with common temperature compensation. Their measurement range was ±60000 με, maximum resolution was 0.1 με, and specified system uncertainty was no greater than 0.5% ± 3 με. Gauge bonding was completed after all strings had been unloaded. The acquisition units were then connected, followed by bridge balancing and zero acquisition. Measurements were collected with the piano fully tuned and repeated at consecutive stabilized states.

Eighty-seven resistance gauges were installed in total, comprising 77 measurement gauges and 10 gauges for temperature compensation. The measurement set included 20 three-element strain rosettes, accounting for 60 channels, together with 17 single gauges. Figure 1 shows that most measurement positions lay on ribs

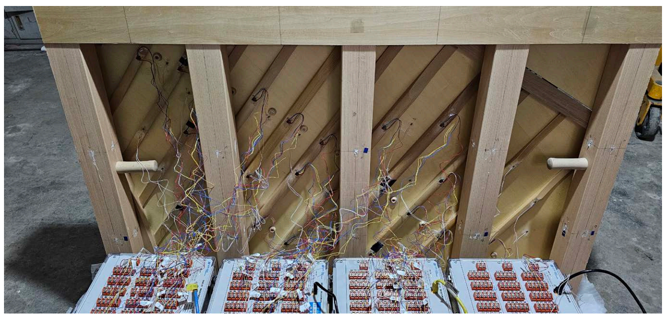

(a)

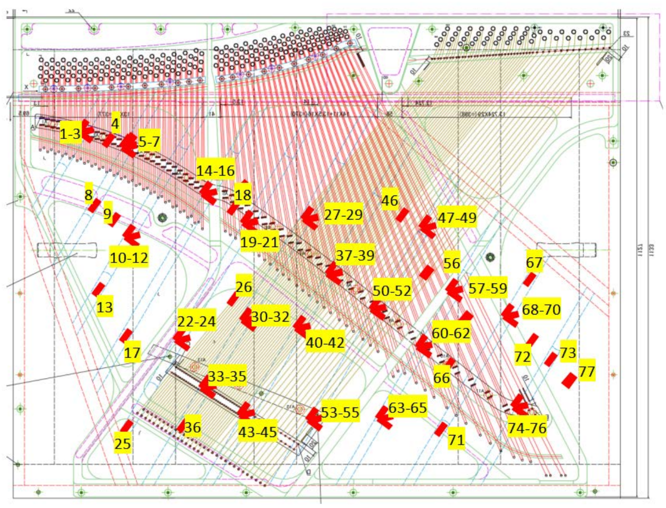

(b)

Figure 1. Electrical strain-measurement arrangement for the UH121 soundboard. (a) Rib-side installation of resistance gauges and measurement leads connected to four DH3818Y acquisition units; (b) Measurement-channel locations on the soundboard, with labels indicating channel numbers. The correspondence between rosette channels and measurement directions is listed in Table 3.

opposite the bridge regions. A single gauge followed either the parallel or perpendicular direction of its local rib. With the local x-axis defined parallel to the rib, the first, second, and third ascending channel numbers in a rosette corresponded to ε_{90} (rib-perpendicular), ε_{45}, and ε_0 (rib-parallel), respectively [19]. Single-gauge channels were numbered 4, 8, 9, 13, 17, 18, 25, 26, 36, 46, 56, 66, 67, 71, 72, 73, and 77. Channel 26 was faulty and was removed from the dataset, leaving 76 valid measurement channels. Table 3 lists the full relationship between each rosette and its channel numbers.

Table 3. Strain-rosette identifiers and measurement-channel distribution.

Rosette	ε_{90}: Perpendicular to Rib	ε_{45}: 45˚ to Rib	ε_0: Parallel to Rib
R1	1	2	3
R2	5	6	7
R3	10	11	12
R4	14	15	16
R5	19	20	21
R6	22	23	24
R7	27	28	29
R8	30	31	32
R9	33	34	35
R10	37	38	39
R11	40	41	42
R12	43	44	45
R13	47	48	49
R14	50	51	52
R15	53	54	55
R16	57	58	59
R17	60	61	62
R18	63	64	65
R19	68	69	70
R20	74	75	76

2.9. Regional Comparison of Finite-Element and Electrical Measurement Results

For a pointwise comparison to be meaningful, numerical and measured strains must share the same location, structural surface, and sensing direction. If n denotes a unit vector along the gauge axis, the finite-element strain projected in that direction is

$$\varepsilon_g = n^{\mathrm{T}} \varepsilon n \tag{5}$$

Equation (5) resolves the finite-element strain tensor along the gauge axis and thus gives the axial strain comparable with a resistance-gauge reading [17] [19]. Here, high-response measurements were assessed against the principal-strain and principal-stress fields by considering their location, tensile or compressive sign, and approximate magnitude. The comparison was regional, since an error computed between unpaired global extrema would not represent a pointwise numerical-experimental difference.

In the present study, however, gauge-oriented finite-element strains were not extracted at the measurement coordinates. Equation (5), therefore, states the projection required for a future pointwise comparison rather than a calculation implemented in the current dataset; no pointwise finite-element-to-gauge prediction errors are reported.

The electrical strains were converted to nominal stress using $E = 14.15$ GPa and $\nu = 0.328$, consistent with the finite-element elastic inputs. To reduce the influence of this shared material assumption, the regional comparison emphasized gauge location, orientation, and tensile/compressive character, while the converted stresses were used only to describe response magnitude.

2.10. Data and Model Availability

The complete Workbench/Mechanical model contains restricted product geometry and engineering information and is therefore not publicly released. To permit technical assessment of the work, the paper reports the software, element type, mesh size, material representation, boundary condition, load definition, solution settings, and principal derived results. Subject to the relevant permissions, authorized derived data may be made available.

3. Results

3.1. Model and Load Mapping

The UH121 model retained the soundboard, ribs, and treble and bass bridges without symmetry reduction (**Figure 2(a)**, **Figure 2(b)**), while the peripheral support region constrained all translational degrees of freedom (**Figure 2(c)**). For full-string static loading, every one of the 438 source points was transferred to a bridge surface. Source and target global Z-resultants were identical at −6413.5 N, with a scale factor of 1.0 (**Figure 2(d)**). Direct summation of the 1,882 F_Z commands gave −6413.464969 N, only 0.000546% away from the interface value. The resultant force was therefore conserved by the imported-load mapping.

3.2. Mesh Independence and Global Z-Direction Bending

Maximum total deformation over the three meshes lay between 1.4251 and 1.5045 mm, and the largest difference from the fine-mesh result was 3.40%. More importantly, neither the high-deformation zone nor the overall bending pattern shifted appreciably with refinement, so the global deformation showed limited mesh sensitivity. With the baseline mesh, maximum total deformation reached 1.5045 mm (**Figure 3(a)**, **Figure 3(b)**), and global Z displacement ranged from

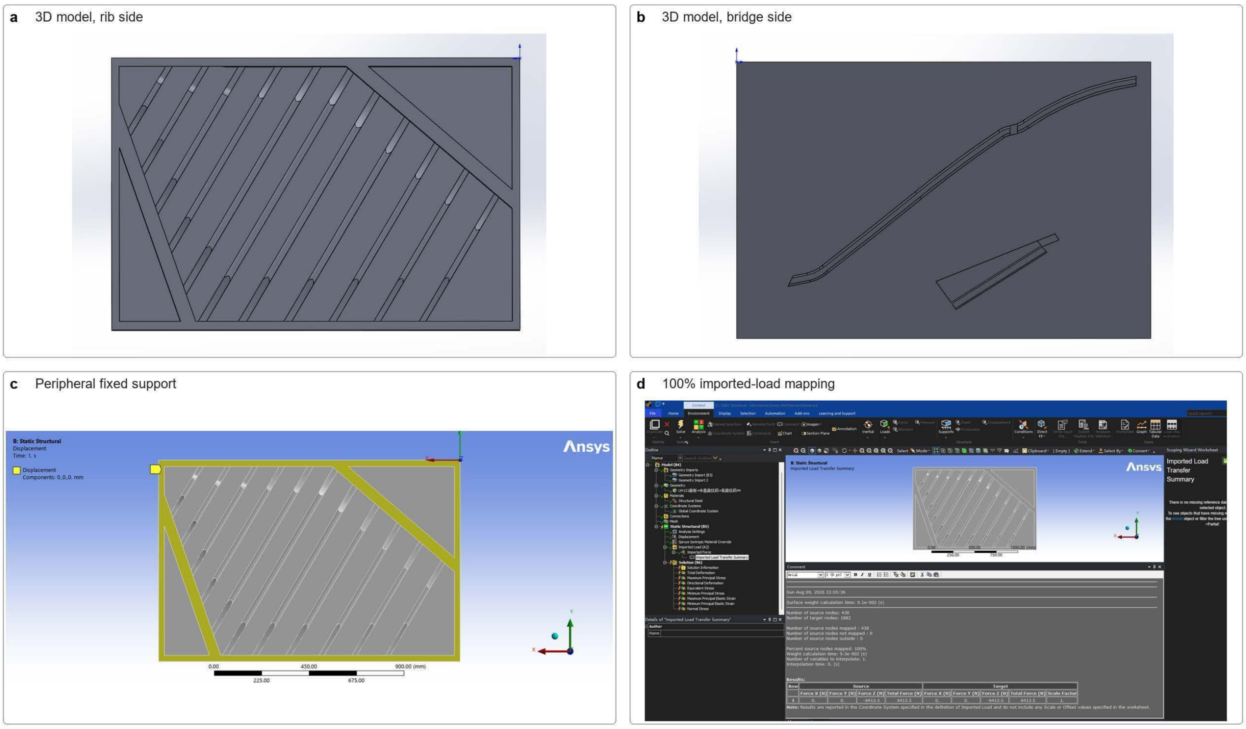

Figure 2. UH121 soundboard model, boundary condition, and imported load. (a) Three-dimensional model viewed from the rib side; (b) Model viewed from the bridge side; (c) Peripheral fixed support; (d) 100% imported-load mapping. All 438 source points were mapped, and the source and target Z-resultants were both −6413.5 N.

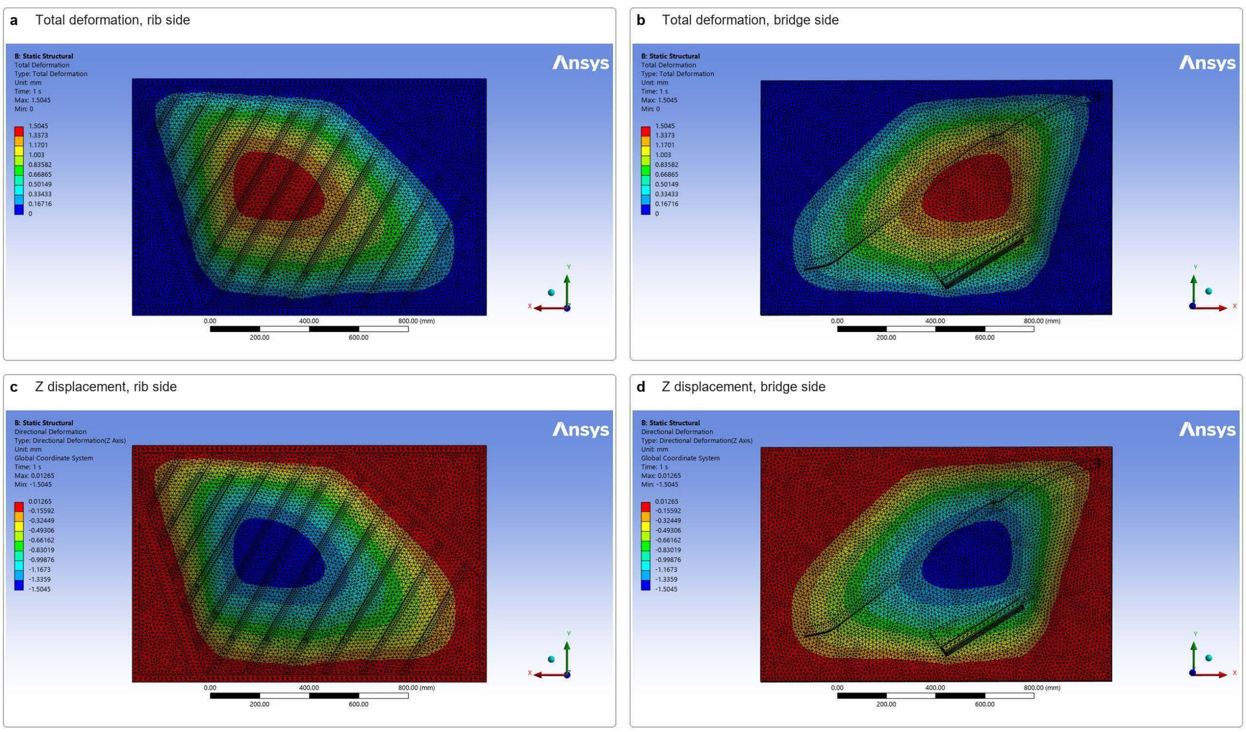

Figure 3. Static deformation under the mapped full-string static downbearing. (a) (b) Total deformation on the rib and bridge sides, respectively; (c) (d) Global Z-direction displacement on the rib and bridge sides, respectively. The maximum total deformation was 1.5045 mm, and the Z displacement ranged from −1.5045 to 0.01265 mm.

−1.5045 to 0.01265 mm (Figure 3(c), Figure 3(d)). The largest downward Z displacement was almost identical in magnitude to the maximum total deformation, which identifies Z-direction bending as the dominant global response. A broad, continuous downward-displacement region covered the main soundboard area, while its contours changed locally where they crossed rib projections.

3.3. Principal Stress and Strain Localization

Principal stress reached a maximum of 17.894 MPa and a minimum of −22.151 MPa (Figure 4); in magnitude, the compressive peak was about 1.24 times the tensile peak. The strongest responses appeared mainly around the bridges, ribs, bridge-rib neighborhoods, and constrained perimeter, rather than coinciding with the location of maximum displacement. A maximum equivalent stress of 20.548 MPa was also obtained (Table 4), but this field was used only to indicate localized multiaxial response.

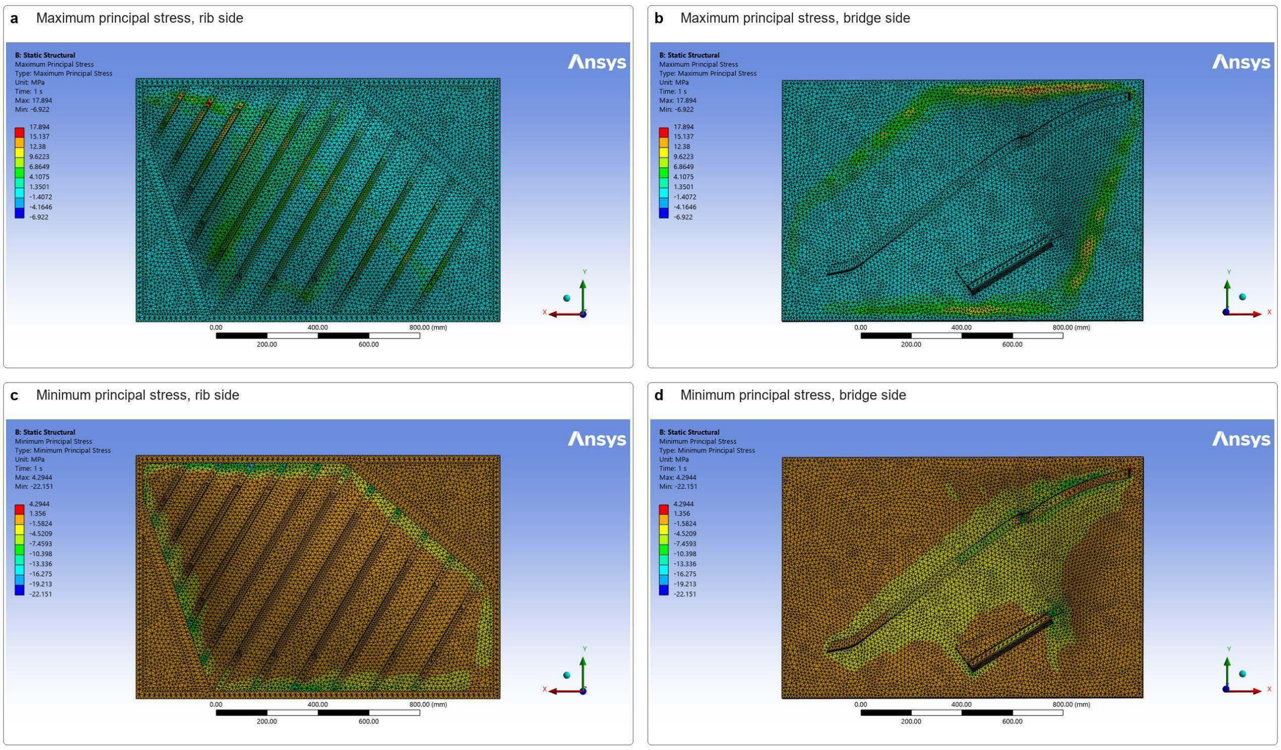

Figure 4. Principal-stress distributions. (a) (b) Maximum principal stress on the rib and bridge sides, respectively; (c) (d) Minimum principal stress on the rib and bridge sides, respectively. The extrema were 17.894 and −22.151 MPa. Principal stress is used to identify high-response regions and not as a material-failure criterion.

The principal elastic-strain extrema were 1,264.4 and −1,420.2 με (Figure 5). Localized bands in the principal-strain maps followed the bridge and bridge-rib regions, where principal-stress concentrations also appeared. Reading the displacement, stress, and strain fields together gives a coherent transfer sequence: load enters through the bridges, spreads through the soundboard and adjacent ribs, and continues toward the constrained perimeter. These connected response regions, rather than a single isolated maximum, define the main load paths in the baseline model.

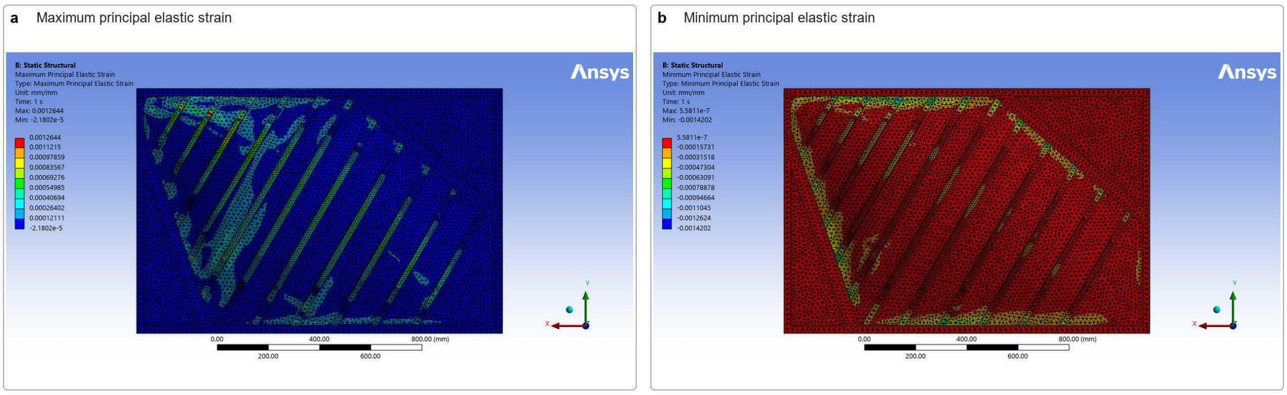

Figure 5. Principal elastic-strain distributions. (a) Maximum principal elastic strain; (b) Minimum principal elastic strain. The extrema were 1264.4 and −1420.2 με.

Table 4. Principal outputs of the 100%-mapped baseline model.

Quantity	Value	Physical Interpretation
Source/target F_Z	−6413.5/−6413.5 N	Conservation of the mapped resultant
Maximum total deformation	1.5045 mm	Global deformation magnitude
Z displacement	−1.5045 to 0.01265 mm	Global bending response
Maximum/minimum principal stress	17.894/−22.151 MPa	Local tensile/compressive response regions
Maximum/minimum principal strain	1264.4/−1420.2 με	Local strain-concentration regions
Maximum equivalent stress	20.548 MPa	Auxiliary multiaxial-stress indicator

3.4. Electrical Strain-Measurement Results

The electrical experiment used 77 measurement channels distributed among 20 three-element rosettes and 17 single gauges. Excluding faulty channel 26 left 76 valid channels. Within each rosette, ascending channel numbers represented ε_{90}, ε_{45}, and ε_0 in that order, corresponding to rib-perpendicular, 45˚, and rib-parallel directions (Table 3). Rosette 16 occupied channels 57 - 59, and rosette 17 occupied channels 60 - 62; channels 57 and 60 were consequently both rib-perpendicular ε_{90} measurements.

Nominal stresses converted from the electrical strain readings were 11.30 MPa in tension at channel 57 and −6.56 MPa in compression at channel 60. The two rosettes lay on the same rib near the junction of the medium-to-high and bass string groups. Between consecutive stabilized measurements, channel 57 decreased by 0.26 MPa, or approximately 2.25%, while channel 60 changed by −0.02 MPa, approximately 0.31% in magnitude. This experimentally observed high-response region occupied the same general bridge-rib and local transfer area highlighted by the finite-element fields.

Three measurement sessions were available. After excluding faulty channel 26, 76 valid channels remained. The final two consecutive stabilized states gave mean absolute stresses of 3.151 and 3.019 MPa. Across the 76 paired channels, Pearson's r was 0.99849; the mean third-minus-second difference was −0.224 MPa (SD 0.213 MPa; 95% CI −0.273 to −0.175 MPa), the mean absolute difference was 0.252 MPa, and the root-mean-square difference was 0.309 MPa. The largest absolute change was 0.75 MPa. These statistics describe short-term agreement between two stabilized measurement sessions and do not represent independent-specimen repeatability.

3.5. Regional Numerical-Experimental Comparison

Bridge-rib neighborhoods emerged as high-response regions in the finite-element principal-stress and principal-strain fields; pronounced tensile and compressive readings were also obtained experimentally within the same part of the structure. The comparison was regional, based on spatial distribution and response sign. Gauge-oriented finite-element values at channels 57 and 60 were not available; the model-wide principal extrema were therefore not treated as matched predictions, and no pointwise errors were calculated. Agreement in the location of high-response regions provides qualitative experimental support for the local load-transfer pattern predicted by the model.

4. Discussion

4.1. Principal Findings

The UH121 soundboard displayed a clear separation between its global and local static responses under full-string downbearing. Maximum total deformation nearly matched the magnitude of the greatest downward Z displacement, showing that transverse bending governed the overall motion. The largest principal stress and strain magnitudes, by contrast, clustered around bridges, ribs, bridge-rib neighborhoods, and the constrained perimeter rather than around the maximum-deflection point. Electrical measurements also detected a pronounced response on a rib near the intersection of string groups, within a high-response area of the finite-element fields. The combined evidence depicts the bridges as load-entry components and the soundboard-rib structure as the path by which that load is redistributed toward the perimeter.

4.2. Global Bending and Local Load Redistribution

Two structural behaviors can be distinguished in the response fields, even though they arise from the same applied load. The broad Z-displacement region expresses the bending compliance of the assembly as a whole, whereas narrow stress and strain bands identify sharper stiffness transitions and local redistribution. In this setting, the ribs do more than raise global stiffness: their projections alter nearby deformation contours, and the surrounding material participates in the localized stress and strain fields. The bridges likewise have a dual role, receiving the mapped downbearing at their surfaces while providing relatively stiff routes into the panel and ribs.

Earlier piano-soundboard studies provide a useful mechanical context for this spatial pattern. Berthaut *et al*. [6] found that realistic structural prediction depends on explicit representation of the panel, ribs, bridges, and material directions. Trévisan *et al*. [4] [9] related the partitioning of ribbed orthotropic panels to rib arrangement, while Chaigne *et al*. [2] connected ribs with the spatial localization of the response. Their analyses were mainly dynamic, yet the underlying observations about stiffness distribution and structural partitioning are compatible with the static fields obtained here.

4.3. Downbearing, Material Representation, and Geometric Effects

No resultant-force loss occurred during imported-load transfer, as shown by the identical source and target resultants. More elaborate piano-soundboard models have included initial crown, downbearing, and geometric stiffness [12], and Corradi *et al*. [14] also represented orthotropic behavior and manufacturing stress. The present calculation instead uses a linear-static description without manufacturing prestress, self-weight, or the tuning sequence. Its results should consequently be read as a static baseline for the existing rib layout and prescribed geometry under vertical downbearing.

The choice of material representation also shapes the meaning of the local results. Direction-dependent spruce properties, often with separate parameter sets for panel, ribs, and bridges, have been used in earlier piano-soundboard models [6] [11] [12] [14]. Here, a common isotropic effective modulus of 14.15 GPa and Poisson's ratio of 0.328 established a uniform structural baseline. That simplification suppresses the longitudinal-transverse stiffness contrast of wood and can influence local strain direction and stress redistribution. For this reason, local maxima are interpreted through the extent and continuity of the surrounding field, not as self-sufficient nodal quantities.

4.4. Interpretation of the Experimental Comparison

Electrical strain measurement adds an independent regional view of the high-response area predicted numerically. The selected tensile and compressive channels belonged to rosettes on the same rib near the intersection of string groups, within a principal load-transfer region of the computed fields. Across all 76 valid channels, the final two consecutive stabilized states yielded Pearson's $r = 0.99849$, a mean third-minus-second difference of −0.224 MPa (SD 0.213 MPa; 95% CI −0.273 to −0.175 MPa), and a mean absolute difference of 0.252 MPa. These statistics indicate short-term agreement between two stabilized measurement sessions; they do not represent independent-specimen repeatability.

Sampling and direction must be kept in view when reading the numerical-experimental comparison. Principal strain is an eigenvalue of the strain tensor, whereas a resistance gauge records normal strain only along its own axis. The finite-element extrema also cover the complete model, unlike the discrete experimental positions. Accordingly, the comparison uses the spatial distribution and tensile/compressive character of responses within the same structural region; differences between unpaired global extrema are not reported as prediction errors. Equation (5) provides the required projection when gauge-oriented finite-element strain is needed.

Several factors could contribute to differences in numerical and measured magnitude, including material anisotropy, boundary stiffness, manufacturing state, load idealization, local geometry, and gauge orientation. The available regional comparison does not separate those effects, but it does identify locations where both datasets consistently show a strong response.

4.5. Engineering Relevance

At the scale of the complete UH121 rib-soundboard-bridge structure, the baseline model captures both overall compliance and localized response. Maximum deflection occurs away from several stress/strain concentrations, which means that global displacement alone is insufficient for static assessment. Bridge-rib neighborhoods and comparable stiffness-transition regions deserve particular attention when rib design, local reinforcement, or the placement of future measurements is considered.

The present analysis supplies a static reference for the existing structure; it does not compare competing rib designs. Rib spacing, cross-section, orientation, and local stiffness can later be examined with the same loading and response measures. Since only static behavior was modeled, no inference is made here about tone, modal properties, or sound radiation.

4.6. Limitations and Future Work

The scope of the conclusions is bounded by several modeling choices. Isotropic linear elasticity and an idealized fixed perimeter were used, whereas orthotropic wood behavior, adhesive compliance, manufacturing prestress, self-weight, and the tuning sequence were omitted. The three-level mesh comparison showed a stable global displacement field, although isolated local stress peaks may still depend on discretization; load transfer was therefore read from continuous field patterns. Electrical measurements were compared with the finite-element response by region rather than by calculating pointwise errors for every gauge. These restrictions matter most when interpreting local maxima and numerical prediction error, while the reported global bending pattern and high-response regions remain direct descriptive outputs of the baseline model.

Because no compliant-boundary calculation was available, local extrema near the perimeter should be considered boundary-condition dependent. Likewise, the experiment supports only a regional response pattern in the current dataset; quantitative validation awaits gauge-coordinate mapping and gauge-oriented strain-tensor projection.

A pointwise axial-strain comparison would require the gauge coordinates and sensing directions to be mapped onto the finite-element surface. Further model development could also introduce orthotropic properties, compliant connections, an initial crown, and manufacturing prestress. With those additions, alternative rib configurations could be compared within a common loading framework, with tighter control over the numerical-experimental correspondence.

5. Conclusions

Full-string static downbearing produced a UH121 soundboard response governed globally by Z-direction bending. Locally, principal stress and strain are concentrated around the bridges, ribs, bridge-rib neighborhoods, and peripheral support. The pattern indicates that the bridges introduced the string load and that the panel and ribs then redistributed it through the assembly. Electrical strain measurements located a high response in the same general structural region, providing qualitative support for the spatial pattern predicted by the finite-element model.

Maximum deflection and the principal local stress/strain concentrations did not occur at the same position, so a single response quantity cannot adequately describe the static state of the soundboard. The three-level mesh comparison supported the stability of global deformation. Taken together, the baseline calculation and the observed division between global bending and local redistribution provide a reference for gauge-oriented comparison, more detailed material descriptions, and later investigations of rib configuration.

Author Contributions

Conceptualization: Wei Xiao and Chengzhong Gong; Methodology: Wei Su. All authors reviewed and approved the final manuscript.

Acknowledgements

The authors thank Yihua Li and Zhenhao Shi for their contributions to model development and experimental work.

Conflicts of Interest

The authors declare no conflicts of interest regarding the publication of this paper.

References

[1] Boutillon, X. and Ege, K. (2013) Vibroacoustics of the Piano Soundboard: Reduced Models, Mobility Synthesis, and Acoustical Radiation Regime. *Journal of Sound and Vibration*, **332**, 4261-4279. https://doi.org/10.1016/j.jsv.2013.03.015

[2] Chaigne, A., Cotté, B. and Viggiano, R. (2013) Dynamical Properties of Piano Soundboards. *The Journal of the Acoustical Society of America*, **133**, 2456-2466. https://doi.org/10.1121/1.4794387

[3] Ege, K., Boutillon, X. and Rébillat, M. (2013) Vibroacoustics of the Piano Soundboard: (Non)linearity and Modal Properties in the Low- and Mid-Frequency Ranges. *Journal of Sound and Vibration*, **332**, 1288-1305. https://doi.org/10.1016/j.jsv.2012.10.012

[4] Trévisan, B., Ege, K. and Laulagnet, B. (2016) Vibroacoustics of Orthotropic Plates

Ribbed in Both Directions: Application to Stiffened Rectangular Wood Panels. *The Journal of the Acoustical Society of America*, **139**, 227-246. https://doi.org/10.1121/1.4939706

[5] Elie, B., Cotté, B. and Boutillon, X. (2022) Physically-Based Sound Synthesis Software for Computer-Aided-Design of Piano Soundboards. *Acta Acustica*, **6**, Article No. 30. https://doi.org/10.1051/aacus/2022024

[6] Berthaut, J., Ichchou, M.N. and Jézéquel, L. (2003) Piano Soundboard: Structural Behavior, Numerical and Experimental Study in the Modal Range. *Applied Acoustics*, **64**, 1113-1136. https://doi.org/10.1016/s0003-682x(03)00065-3

[7] Klímová, H. and Tippner, J. (2014) Modal Analysis of Soundboard of the Upright Piano by Finite Element Method (FEM). *Wood Research*, **59**, 123-136. https://www.woodresearch.sk/wr/201401/11.pdf

[8] Li, P., Tao, Y.B. and Shi, S.Q. (2014) Modal Analysis of Upright Piano Soundboards by Combining Finite Element Analysis and Computer-Aided Design. *Wood and Fiber Science*, **46**, 376-384.

[9] Trévisan, B., Ege, K. and Laulagnet, B. (2017) A Modal Approach to Piano Soundboard Vibroacoustic Behavior. *The Journal of the Acoustical Society of America*, **141**, 690-709. https://doi.org/10.1121/1.4974860

[10] Trévisan, B., Ege, K. and Laulagnet, B. (2017) Vibroacoutsic Modelling of Piano Soundboards through Analytical Approaches in Frequency and Time Domains. In: *Conference Proceedings of the Society for Experimental Mechanics Series*, Springer, 77-80. https://doi.org/10.1007/978-3-319-54858-6_8

[11] Valiente, P.M., Squicciarini, G. and Thompson, D.J. (2024) Influence of Soundboard Modelling Approaches on Piano String Vibration. *The Journal of the Acoustical Society of America*, **155**, 3213-3232. https://doi.org/10.1121/10.0025925

[12] Mamou-Mani, A., Frelat, J. and Besnainou, C. (2008) Numerical Simulation of a Piano Soundboard under Downbearing. *The Journal of the Acoustical Society of America*, **123**, 2401-2406. https://doi.org/10.1121/1.2836787

[13] Mamou-Mani, A., Le Moyne, S., Ollivier, F., Besnainou, C. and Frelat, J. (2012) Prestress Effects on the Eigenfrequencies of the Soundboards: Experimental Results on a Simplified String Instrument. *The Journal of the Acoustical Society of America*, **131**, 872-877. https://doi.org/10.1121/1.3651232

[14] Corradi, R., Miccoli, S., Squicciarini, G. and Fazioli, P. (2017) Modal Analysis of a Grand Piano Soundboard at Successive Manufacturing Stages. *Applied Acoustics*, **125**, 113-127. https://doi.org/10.1016/j.apacoust.2017.04.010

[15] Mokdad, F. and Missoum, S. (2014) A Fully Parameterized Finite Element Model of a Grand Piano Soundboard for Sensitivity Analysis of the Dynamic Behavior. *Proceedings of the ASME International Design Engineering Technical Conferences*, Buffalo, 17-20 August 2014, V008T13A072.

[16] Corradi, R., Fazioli, P., Marforio, S., Paluello, A., Ripamonti, F. and Squicciarini, G. (2010) Modal Analysis of a Grand Piano Soundboard. *Proceedings of ISMA* 2010, Leuven, 20-22 September 2010, 59-72.

[17] Bower, A.F. (2009) Applied Mechanics of Solids. CRC Press.

[18] ANSYS Inc (n.d.) Mechanical APDL Theory Reference: Structural Fundamentals and Stress-Strain Relationships. ANSYS Documentation.

[19] Micro-Measurements (n.d.) Strain Gage Rosettes: Selection, Application and Data Reduction (Technical Note TN-515). https://micro-measurements.com/knowledge-base/technical-notes